Edinburgh Research Explorer

# Solar chimney power plant integrated with a photocatalytic reactor to remove atmospheric methane: A numerical analysis

# Solar chimney power plant integrated with a photocatalytic reactor to remove atmospheric methane: a numerical analysis

Tingzhen Ming[1,2], Haoyu Gui[1], Tianhao Shi[1], Hanbing Xiong[1], Yongjia Wu[1,] *, Yimin Shao[3],
Wei Li[3]*, Xiaohua Lu[4], Renaud de Richter[5]

1. School of Civil Engineering and Architecture, Wuhan University of Technology, No.122 Luoshi Road, Hongshan District, Wuhan, 430070, China

2. School of Architectural Engineering, Huanggang Normal University, No. 146 Xingang Second Road, Huanggang 438000 China

3. Institute for Materials and Processes, School of Engineering, The University of Edinburgh, Edinburgh EH9 3FB, Scotland, UK

4. College of Chemical Engineering, State Key Laboratory of Materials-oriented Chemical Engineering, Nanjing Tech University, Nanjing, 211816, PR China

5. Tour-Solaire.Fr, 8 Impasse des Papillons, F34090 Montpellier, France

**Abstract**: Methane ($CH_4$) is the second largest contributor to global warming among all greenhouses gases. A solar chimney power plant integrated with a photocatalytic reactor (SCPP-PCR) is a promising large-scale method for removing $CH_4$ from the atmosphere. This study used computational fluid dynamics (CFD) to investigate the performance and factors influencing photocatalytic oxidation of methane by the SCPP-PCR system. The geometry of a SCPP is the same as the prototype of the SCPP built in Manzanares (Spain). The PCR is designed based on a honeycomb monolith photoreactor. The numerical results revealed that the SCPP-PCR system degraded 21,312 g methane per day with the actual solar radiation data when the channel diameter of the honeycomb PCR was 4 mm and channel length was 8 m. Although increasing the length or decreasing the channel diameter of the PCR would improve photocatalytic efficiency, the rate of airflow of the system would be reduced. The maximum methane purification rate of the SCPP-PCR system was determined.

**Keywords:** Non-$CO_2$ greenhouse gas removal, photocatalytic reactor, Solar chimney power plant, Numerical simulation, global warming

| | | | |
|---|---|---|---|
| **Nomenclature** | | | |
| $a$ | Thermal diffusivity($m^2/s$) | $Ra$ | Rayleigh number |
| $B, B_1, B_2$ | Constants for measured experimentally | $R_m$ | Volume reaction rate of methane photocatalysis ($mol\cdot m^{-3}\,s^{-1}$) |
| $C_{1\varepsilon}$, $C_{2\varepsilon}$, $C_{3\varepsilon}$ | Constants for turbulent model | $R_p$ | Purification rate ($g/s$) |
| $C$ | Inertia coefficient | $r_{AI}$ | Reaction rate per absorbed irradiation intensity and unit of catalyst surface ($mol\cdot W^{-1}s^{-1}$) |
| $c_1$ | ~~Methane~~ Mole concentration of Methane ($mol/m^3$) | $S$ | Surface area of porous media zone ($m^2$) |
| $c_2$ | Mole concentration of Oxygen ~~concentration~~ ($mol/m^3$) | $S_\Phi$ | Momentum loss term |
| $c_p$ | Specific heat at constant pressure ($J/(kg\ K)$) | $S_i$ | Extra rate due to the discrete phase |
| $D_P$ | Pore diameter of porous media (i.e. channel diameter of honeycomb monolith PCR) ($mm$) | $SSA$ | Specific surface area ($m^2$) |
| $E_s$ | Photocatalytic efficiency | $t$ | Time ($s$) |
| g | Acceleration of gravity ($m/s^2$) | $T$ | Temperature ($K$) |
| $G$ | Solar radiation intensity ($W/m^2$) | $T_0$ | Ambient temperature ($K$) |
| $G_k$ | Turbulence kinetic energy generation due to the mean velocity gradients ($J$) | $u$ | Average velocity magnitude in the axial direction ($m/s$) |
| $G_b$ | Turbulence kinetic energy generation due to turbulence ($J$) | $V$ | Apparent volume of porous media zone ($m^3$) |
| $H$ | Collector height ($m$) | $x, y, z$ | Cartesian space coordinates |
| $\vec{J_\iota}$ | Diffusion flux of species $i$ ($mol/(s\cdot m^3)$) | | |
| | | ***Greek symbols*** | |
| $J_1$ | Mole fraction of Methane at system entrance ($ppb$) | $v$ | Kinetic viscosity($m^2/s$) |
| $J_2$ | Mole fraction of Methane at system exit ($ppb$) | $\beta$ | Volume coefficient of expansion ($1/K$) |
| $K$ | Permeability | $\rho$ | Air density ($kg/m^3$) |
| $L$ | Length of PCR (i.e. channel length of honeycomb monolith) ($m$) | $\tau$ | Shear stress caused by viscosity ($N/m^2$) |
| $p$ | pressure ($Pa$) | $k$ | Karman constant |
| $q$ | Heat flux through the ground underneath the collector ($W/m^2$) | $\gamma$ | Porosity |

# 1. Introduction

32    The "21st United Nations Climate Change Conference" held in Paris in December

33    2015 agreed to a global response to climate change after 2020. The Paris Agreement

34    aimed to control the rise in average global temperature 1.5–2°C lower than the pre-

35    industrial level. This is an ambitious task requiring a rapid decrease in greenhouse gas

36    (GHG) emissions. However, in some sectors, e.g., agriculture and aviation, it is difficult

37    to eliminate GHG emissions entirely. We must develop technologies to remove GHGs

38    from the atmosphere on a large scale [1].

39    $CO_2$ is the most significant contributor to global warming among all GHGs. Thus,

40    it is the primary focus of most GHG removal research. To date, little attention has been

41    given to the removal of atmospheric non-$CO_2$ GHGs [2]. The global warming potential

42    (GWP) is a measure of the potency of a GHG. Many non-$CO_2$ atmospheric gases have

43    a high GWP. For example, methane ($CH_4$) has a 27–35 times higher GWP than $CO_2$

44    over 100 years which represents almost 25% of the radiative forcing of long-lived

45    (lifetime $\geq$ 10 years) GHGs.

46    The technology of semiconductor photocatalysis (PC) has shown broad prospects

47    in the field of GHG conversion and pollutant degradation in recent years [3-5].

48    Mohamedali et al. [6] proposed converting methane to oxygenated hydrocarbons or

49    syngas as an attractive way to mitigate the greenhouse effect. Krishna et al. [7] used

50    uranyl-anchored MCM-41 as a heterogeneous photocatalyst to confirm the high activity

51    of total oxidation of methane to carbon dioxide at room temperature under sunlight. In

52    et al. [8] investigated the photocatalytic performance of methane decomposition over

53    vertically aligned $TiO_2$ nanotube arrays. According to the experimental results, the

54    optimal thickness of the photocatalyst for methane oxidation was about 575 nm under

55    367-nm illumination. Chen et al. [9] provided a two-step photocatalytic reaction

56    process to explain the photocatalytic oxidation of methane. Temperature fluctuations

57    had little effect on methane photo-oxidation, and the reaction process proceeded faster

58    at lower methane concentrations, demonstrating the prospects of photocatalytic

59    oxidation for atmospheric methane degradation. In general, most methane PS research

60    is in the laboratory stage. Only a few studies have been conducted outdoors due to

61 numerous uncontrollable factors in the outdoor photocatalysis process. Some $NO_x$

62 outdoor photocatalytic experiments can be found in the literature [10-11].

63     Methane is photocatalytically transformed into water vapor and $CO_2$, and the

64 potency of the GHGs is significantly lower than the precursor [12].

65 $CH_4 + 2O_2 \rightarrow 2H_2O + CO_2$;
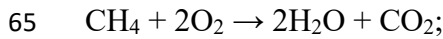
66     This PC process allows for harnessing sunlight to promote the destruction of $CH_4$,

67 and has been proven very effective on a laboratory scale [9]. However, process

68 intensification is needed for methane removal at a climatically relevant scale, which

69 requires sufficient airflow given the extreme dilution of methane. Significant airflow

70 must be collected, processed under well-controlled parameters (i.e., light intensity, wind

71 speed and direction, and relative humidity), and monitored in-situ.

72     de Richter et al. first proposed a novel technology of combining a solar chimney

73 power plant (SCPP) with PC [13]. This is an emerging technology for non-$CO_2$ GHG

74 removal discovered in two of the latest reports from the Intergovernmental Panel on

75 Climate Change [14] and the Royal Society [1].

76     The idea of the SCPP was proposed by Schlaich in 1978, and the first 50 kW SCPP

77 prototype was built and successfully operated in Manzanares, Spain in the 1980s, also

78 known as the Manzanares pilot plant [15]. Subsequently, a growing number of

79 researchers engaged in SCPP research, and the development of this technology was

80 summarized in several reviews [16-19]. A conventional SCPP utilizes the updraft

81 produced by the buoyancy effect to generate electricity. It mainly consists of four

82 essential parts: the collector, the chimney, the energy storage layer, and the turbine. A

83 comprehensive analysis of SCPPs is provided by Bernardes et al. [20]. They described

84 the flow and heat transfer characteristics of an SCPP, and estimated the system power

85 output. Maia et al. [21] analyzed the effects of geometric parameters and the physical

86 properties of the materials on the solar chimney. They found that the tower dimensions

87 were the most significant physical variables to optimize the performance of the SCPP

88 system. Later, Ming et al. [22] discussed the effect of chimney shape on SCPP

89 performance. The influence of the cylindrical chimney tower dimensions on overall

90 system performance was furtherly studied. Guo et al. [23] proposed an analytical

91 approach to evaluate the optimal turbine pressure drop ratio. They discussed the

92 influence of solar radiation and ambient temperature on the optimal turbine pressure

93 drop ratio.

94 SCPP technology is a large-scale renewable energy power generating technology

95 that utilizes the large-scale solar energy resource and produces a large amount of airflow.

96 When solar irradiation intensity and turbine rotational speed are 800 W/m$^2$ and 100

97 r/min, respectively, the 50 kW Manzanares pilot plant provides about 700 m$^3$/s airflow.

98 A 200 MW commercial SCPP provides airflow > 20,000 m$^3$/s. However, due to the low

99 energy conversion efficiency of an SCPP, some innovative SCPP hybrid systems have

100 aroused the interest of researchers. These novel SCPP systems have been applied in

101 various fields, including freshwater generation from air [24, 25], alleviating the

102 problem of urban air pollution [26-28], desalination of seawater with a modified SCPP

103 [29, 30], and improving the partial climate [31, 32].

104 The SCPP-PC is proposed using SCPPs to generate the necessary mass airflow

105 driven only by solar energy [33]. Figure 1 illustrates the operating principle of the

106 SCPP-photocatalytic reactor (PCR) system. The SCPP is comprised of a high chimney

107 at the center of a large solar collector. Strong airflow is generated in the chimney by the

108 buoyance force caused by the heated air under the solar collector. The SCPP can be

109 modified into a giant photocatalytic methane removal system by integrating a PCR

110 under the solar collector.

111 Some challenges of the technology were pointed out in the two latest reports [1, 14]

112 before it can be applied to a large scale. A broader assessment of its effectiveness is

113 lacking. In this study, we evaluated the methane removal effectiveness of an SCPP-

114 PCR system for the first time. Three-dimensional steady numerical simulations of

115 SCPP-PCR with the honeycomb monolith PCR of different pore diameters and channel

116 lengths were carried out. The flow field characteristic and photocatalytic performance

117 of the SCPP-PCR system were studied by analyzing the pressure, velocity and methane

118 concentration distribution inside the system. Then, the effect of solar radiation

119 intensitive on the degradation of atmospheric methane and the system flow performance

120 under the optimum photoreactor dimension were discussed further. This timely work

121 will help to guide the construction of an SCPP-PCR prototype and might provide a

122 game-changing technology for atmospheric-scale methane removal.

123



124
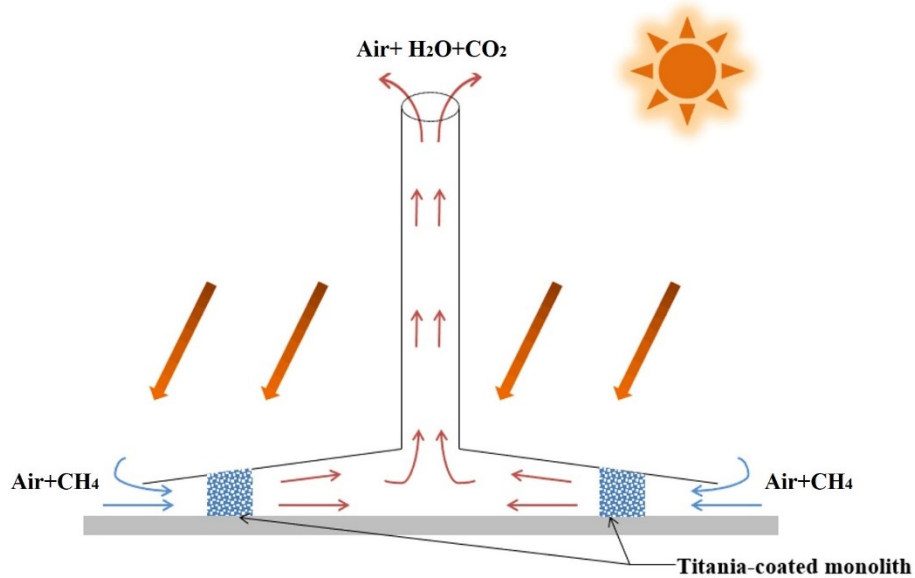
**Fig. 1.** Solar chimney power plant integrated with a photocatalytic reactor (SCPP-PCR) for atmospheric methane removal.

## 2. Model description

*2.1. Geometric Model*

A simplified model was adopted for the numerical analysis to investigate the performance of the SCPP-PCR to remove methane. As shown in Figure 2, the model has a 200-m-high and 5-m-radial chimney with a 120-m radial collector. The collector has a slope in which the height increases from 2 to 6-m from the inlet to the center. As solar radiation is absorbed by the ground, the air inside the collector is continuously heated by the ground surface, resulting in a difference in air density between inside and outside of the system. Due to the stack effect, the air flows upward in the chimney at the center of the collector, and finally flows out of the chimney.

Many types of PCRs are available, such as the plate, tubular, and honeycomb PCRs [34-36]. Different PCR structures can have different specific surface areas, mass

139 transfer rates, and photocatalytic reaction characteristics. The widely studied

140 honeycomb monolith PCR (Figure 3) has a large specific surface area and mass transfer

141 rate. Therefore, this type of PCR was selected to be integrated with the SCPP system.

142 Titanium dioxide ($TiO_2$) is an efficient, stable, cheap, and widely studied photocatalyst

143 [37]. It was selected to be coated on the internal channel surface of the honeycomb

144 monolith PCR. The PCR was located 10-m away from the entrance to the collector. The

145 direction of the honeycomb monolith internal channels was along the path of airflow,

146 ensuring the lowest pressure drop. The height of the PCR was the same as that of the

147 collector, and the channel length of the honeycomb monolith was 3–10-m.
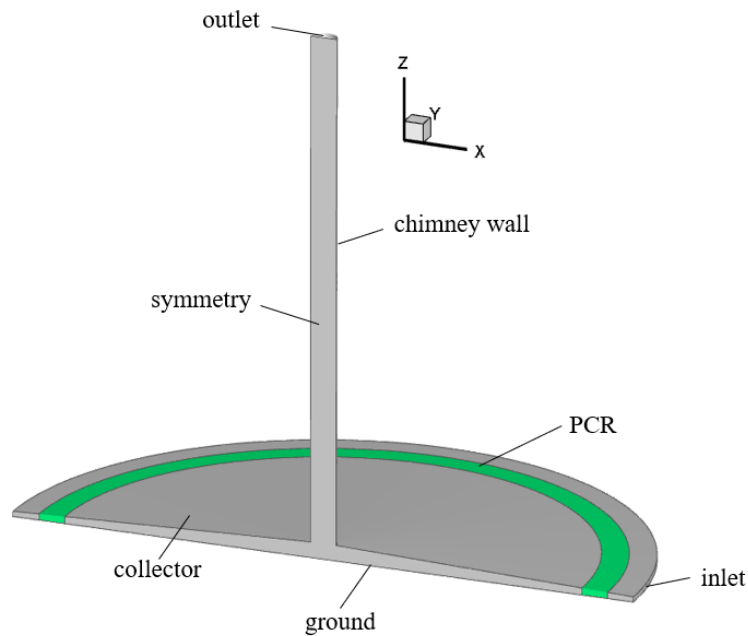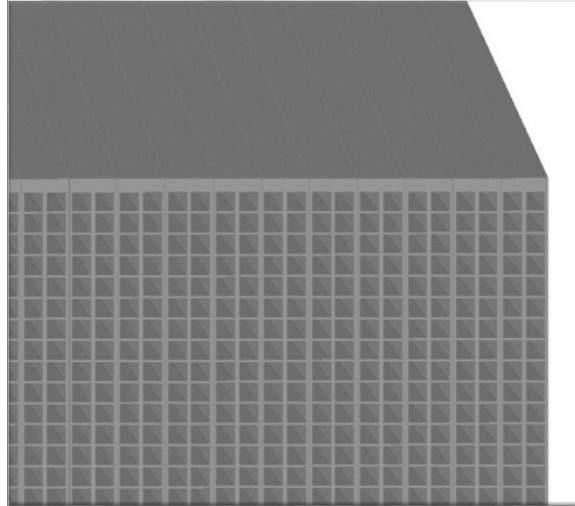
148



149 **Fig. 2.** Three-dimensional geometrical model of the solar chimney power plant integrated

150 with a photocatalytic reactor (SCPP-PCR) system.

**Fig. 3.** Local enlarged image of honeycomb monolith photoreactor.

Because the SCPP-PCR model (as shown in Fig. 2) is symmetric in the XZ plane, only half of the model is used for the numerical simulation. This operation saves computing resources while maintaining the same calculation accuracy [38]. The geometrical model does not consider the effects of the turbine or the energy storage layer. The main purpose of this study is to investigate the photocatalytic performance of the SCPP-PCR and analyze the flow characteristics of fluid in this system.

*2.2. Mathematical Model*

The photocatalytic reaction zone was set as a porous zone and the remainder was set as the fluid zone. According to the flow characteristics of the system, the following assumptions were made:

1) Solar heat radiation energy is steady.

2) The sunlight or artificial light source can be guided to the photocatalytic reaction zone evenly by the side glow optical fibers, ensuring approximately 70% light intensity.

3) Solar thermal radiation is distributed uniformly in the thermal storage layer.

4) No homogeneous chemical reaction occurred.

5) The thickness of the photocatalyst film on the surface of the porous zone is equal.

6) The energy loss in the transition section between the chimney and the collector is not considered.

8

172    The airflow inside a conventional SCPP system is natural convection induced by
173    solar radiation heating the ground surface. The Rayleigh number is a criterion number
174    used to describe the strength of buoyancy-induced flow:

175
$$R_a = \frac{g\beta\Delta T H^3}{av} \tag{1}$$

176    where $g$ is gravitational acceleration, which is 9.81 m/s², $\beta$ is the thermal expansion
177    coefficient, $\Delta T$ is the maximum temperature increase within the system, and $H$, $a$, and
178    $v$ are the collector height, the thermal diffusivity, and the kinematic viscosity,
179    respectively. The Rayleigh number value for the system was higher than $10^{10}$, indicating
180    that fluid flow inside the system is in a vigorous turbulent state. Therefore, the turbulent
181    mathematical model of standard k-ε is selected to describe fluid flow within the system.
182    In addition, the air density changes slightly in the entire calculation model. The error
183    caused by ignoring air compressibility during simulation of a small-scale solar chimney
184    power system, is less than 2% [39]. Thus, the gas phase is assumed to be incompressible,
185    and the ideal gas law is used to express the relationship between density and
186    temperature for natural convection. As a result, the governing equations required for
187    the entire simulation process include: the mass equation, the Navier–Stokes equation,
188    the energy equation standard k-ε equations, and the transport equations, which are
189    written as follows:

190    Continuity equation:

191
$$\frac{\partial \rho}{\partial t} + \frac{\partial(\rho u_i)}{\partial x_i} = 0 \tag{2}$$

192    Navier–Stokes equation:

193
$$\frac{\partial(\rho u_i)}{\partial t} + \frac{\partial(\rho u_i u_j)}{\partial x} = \rho g_i - \frac{\partial p}{\partial x_i} + \frac{\partial \tau_{ij}}{\partial x_j} \tag{3}$$

194    Energy equation:

195
$$\frac{\partial(\rho c_p T)}{\partial t} + \frac{\partial(\rho c_p u_j T)}{\partial x_j} = \frac{\partial}{\partial x_j}\left(\lambda \frac{\partial T}{\partial x_j}\right) + \tau_{ij}\frac{\partial u_i}{\partial x_j} + \beta T\left(\frac{\partial p}{\partial t} + u_j\frac{\partial p}{\partial x_j}\right) \tag{4}$$

196    Equation for the turbulent kinetic energy $k$:

197
$$\frac{\partial(\rho k)}{\partial t} + \frac{\partial}{\partial x_i}(\rho k u_i) = \frac{\partial}{\partial x_j}\left(\alpha_k \mu_{eff}\frac{\partial k}{\partial x_j}\right) + G_k + G_b - \rho\varepsilon - Y_M + S_k \tag{5}$$

198    Equation for the energy dissipation:

9

199 $\frac{\partial}{\partial t}(\rho\varepsilon) + \frac{\partial}{\partial x_i}(\rho\varepsilon u_i) = \frac{\partial}{\partial x_j}\left(\alpha_k\mu_{eff}\frac{\partial\varepsilon}{\partial x_j}\right) + C_{1\varepsilon}\frac{\varepsilon}{k}(G_k + C_{3\varepsilon}G_b) - C_{2\varepsilon}\rho\frac{\varepsilon^2}{k} - R_\varepsilon + S_\varepsilon$ (6)

200 Component transport equation:

201 $\qquad \frac{\partial}{\partial t}(\rho Y_i) + \nabla \cdot (\rho\vec{v}Y_i) = -\nabla \cdot \vec{J_i} + R_i + S_i$ (7)

202 where $\rho, t$, and $c_p$, represent the density, time, and constant-pressure specific heat; $G_k$

203 is the generation of turbulence kinetic energy because of the mean velocity gradients

204 and is defined as $G_k = -\rho\overline{u_i'u_j'}\frac{\partial u_j}{\partial x_i}$, $\sigma_T$、 $\sigma_k$, and $\sigma_\varepsilon$ denote the turbulent Prandtl

205 numbers for $T, k$, and $\varepsilon$ respectively: $\sigma_T = 0.9$, $\sigma_k = 1.0$, $\sigma_\varepsilon = 1.3$. C$_1$ and C$_2$ are

206 two constants for the turbulent model: $C_{1\varepsilon}$=1.44, $C_{2\varepsilon} = 1.92$. $\vec{J_i}$ is the diffusion flux

207 of species $i$: $\vec{J_i} = -\rho D_{i,m} + R_i$, $R_i$ is the net production rate of the chemical reaction,

208 $S_i$ represents the extra rate due to the discrete phase, $Y_M$ represents the contribution

209 of the fluctuating dilatation incompressible turbulence to the overall dissipation rate.

210 To save computational resources, the reaction zone was set as the porous media model

211 instead of introducing a large number of submicron scale meshes for simulation [40].

212 The governing equations describing the inside of the porous media are:

213 Continuity equation:

214 $\qquad \frac{\partial\gamma\rho}{\partial t} + \nabla \cdot (\gamma\rho\vec{v}) = 0$ (8)

215 Navier–Stokes equation:

216 $\qquad \frac{\partial}{\partial t}(\gamma\rho\vec{v}) + \nabla \cdot (\gamma\rho\vec{v}\vec{v}) = -\gamma\nabla p(\gamma\bar{\bar{\tau}}) + \gamma\rho\vec{g} + S_\Phi$ (9)

217 where $\gamma$ is porosity of the porous medium, $\gamma$= 0.85. $\vec{v}$ and $p$ represent the velocity

218 vector of the fluid and pressure, $\bar{\bar{\tau}}$ represents the viscous stress tensor, $\bar{\bar{\tau}} =$

219 $\mu\left[\left(\nabla\vec{v} + \nabla\vec{v}^T - \frac{2}{3}\nabla \cdot \vec{v}I\right)\right]$. $S_\Phi$ denotes the momentum loss term: $S_\Phi = -\left(\frac{\mu}{K}\vec{v} + \right.$

220 $\left. \frac{C_2}{2}\rho|\vec{v}|\vec{v}\right)$, where the first term on the right is the viscous loss term and the second term

221 is the inertia loss term.

222 $\qquad$ The honeycomb structure usually can be represented by a packed bed, and the

223 permeability ($K$) and the inertia coefficient ($C$) in porous media are derived and

224 calculated using the Ergun equation [41]:

225 $$K = \frac{D_P^2}{150} \frac{\gamma^3}{(1-\gamma)^2} \qquad (10)$$

226 $$C = \frac{3.5}{D_P} \frac{(1-\gamma)}{\gamma^3} \qquad (11)$$

227 where $D_P$ is the pore diameter of the porous media.

228 The specific surface area, *SSA,* of the honeycomb structure can be deduced [41]:

229 $$SSA = \frac{(1-\gamma)S}{V} = \frac{6(1-\gamma)\pi D_P^2}{\pi D_P^3} = \frac{6(1-\gamma)}{D_P} \qquad (12)$$

230 where $S$ denotes the surface area of the porous media zone; $V$ represents the apparent

231 volume of the porous media zone.

232 Andreas et al. [42] deduced the surface reaction rate formula of total oxidation of

233 methane by photocatalysis through oxygen-enriched experiments.

234 $$r_{AI} = B \frac{B_1 c_1}{1+B_1 c_1} \frac{B_2 c_2}{1+B_2 c_2} \qquad (13)$$

235 where $r_{AI}$ represents the surface reaction rate of methane photocatalysis; $c_1$ is the

236 concentration of methane; $c_2$ is the concentration of oxygen; and $B$, $B_1$, and $B_2$ are

237 constants measured experimentally. The corresponding values of $B$, $B_1$, and $B_2$ are

238 $5.37 \times 10^{-6}$, 2.42, and 4.60, respectively.

239 Overall, the actual photocatalytic rate $R_m$ in the honeycomb monolith

240 photoreactor was calculated as follows:

241 $$R_m = SSA \times r_{AI} \qquad (14)$$

242 *2.3. Boundary conditions*

243 The domain boundary conditions for computation of the SCPP-PCR are shown in

244 Table. 1. Detailed descriptions of the boundary conditions are as follows. Relative static

245 pressure was used for the simulation to analyze the entire pressure distribution of the

246 system, which is the static pressure difference between the SCPP-PCR and the

247 environment at the same height [43]. The pressures at the entrance to the collector and

248 the chimney outlet were set equal to the standard atmospheric pressure (101,325 Pa)

249 when the height of the SCPP-PCR is relatively low [27]. Namely, the relative static

250 pressure of the collector inlet and chimney outlet was 0. The solar radiation heating the

251 ground surface under the canopy was regarded as heat flux. The energy of absorption

from the soil and the energy lost through thermal radiation and conduction were considered. Solar radiation was set to 857 $W/m^2$, and the corresponding heat flux on the ground surface was set to 600 $W/m^2$, according to typical solar radiation conditions in the deserts of northwest China [44]. Assuming that the ambient air temperature is maintained at 293 K, convective heat transfer will occur on the canopy of the collector with the surrounding air, and it is acceptable for the coefficient of convection to be set to 10 $W/(m^2K)$ when air velocity is not very high [45].

**Table 1.** Boundary conditions.

| Location | Boundary type | Value |
|---|---|---|
| Collector inlet | Pressure inlet | p = 0 Pa, T = 293 K |
| Chimney outlet | Pressure outlet | p = 0 Pa |
| Ground surface | Heat flux | 600 $W/m^2$ |
| Collector canopy surface | convection | T = 293 K, h = 10 $W/(m^2K)$ |
| Chimney wall | Adiabatic wall | 0 $W/m^2$ |
| Symmetry surface | Symmetry | |

*2.4. Simulation method and validation*

The computations were solved by the standard k-ε method and finite-rate reaction model in the general-purpose CFD program ANSYS Fluent 19.2. The numerical calculations were performed with the double precision solver. A simple algorithm was used for the pressure-velocity coupling scheme and the PRESTO! Discrete scheme was applied to discretize the pressure term. The standard wall functions method was used for the near wall region calculation. The QUICK scheme was employed in the discretization of the convective terms and the second-order upwind scheme was used for the discretization of the diffusion terms. Two ways were used to determine solution convergence. First, the maximum residuals of all variables were below $10^{-5}$. Second, the volume flow rate at the chimney outlet remained constant.

As a hexahedral (HEX) meshed grid system is more accurate and effectively avoids the influence of false diffusion on the computational results compared to tetrahedral

275 grids, HEX grids were applied to discretize the computational region.

276 To validate the effectiveness of the numerical simulation in this study, the

277 numerical results were compared with the Spanish prototype using the same parameters.

278 Compared with the Spanish prototype experimental data [46], the maximum

279 temperature difference between the inlet and outlet of the system increased by 4.6%

280 (the impact of ambient crosswind was neglected), but the velocity difference in the

281 chimney was only 0.9%. As is shown in Table 2, the simulation results in this paper

282 were in good agreement with the experimental results from the Spanish prototype.

283 Obviously, this developed numerical model was able to predict the overall performance

284 of SCPP-PCR system accurately.

285

286 **Table 2.**

287 Comparison of simulation results to the experimental data from the Spanish prototype.

| Parameters | Maximum temperature rise (K) | Chimney outlet velocity (m/s) |
|---|---|---|
| Experimental data | 17.5 | 9.10 |
| Calculated value | 18.3 | 9.18 |
| Tolerance | 4.6% | 0.9% |

288

289 Next, three test cases of the model were performed under the same conditions to

290 determine if the numerical simulation results were grid independent. For the three

291 different grid systems (the grid numbers were 1,646,307, 2,083,926, and 2,534,116

292 respectively), the corresponding volume flow rates at the chimney outlet were 885.08,

293 896.32, and 905.63 $m^3$/s respectively. The less than 1.25% deviation demonstrates the

294 grid-independence of simulations in this study. In general, the grid number of the basic

295 mesh model in this paper was 2,083,926.

296 **3. Results and discussion**

297 As explained earlier, the ambient air surrounding the SCPP is continuously

298 transported into the collector through the PCR. The photocatalytic oxidation of methane

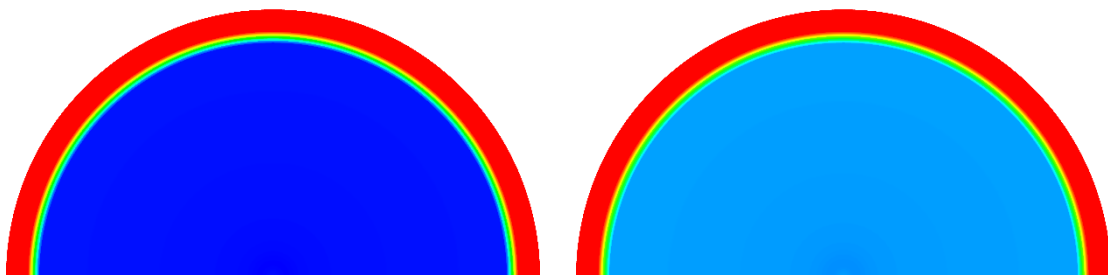299 occurs inside the PCR as air passes through it. Then, the processed air with a lower

13

methane concentration rises inside the chimney and is discharged to high altitude at the chimney exit.

The aim of this study is to investigate the effectiveness of the SCPP-PCR for degrading atmospheric methane and to test the flow performance of the system under different PCR dimensions. In the model, the honeycomb monolith PCR was placed inside the collector 10 m from the entrance to the collector. The PCR was treated as a porous medium. Porosity was 0.85. The pore diameter, $D_P$, of the PCR (i.e., channel diameter) varied from 2 to 4 mm at intervals of 0.5 mm, and the length $L$ of PCR (i.e., channel length) varied from 3 to 10 m at intervals of 1 m. Ambient air temperature, $T_0$, and solar irradiation intensity, $G$, were set to 293 K and 857 W/m$^2$, respectively.

*3.1. Flow performance*

Figure 4 shows the contours of the static pressure distributions at the z = 1 m plane of the SCPP-PCR when $D_P$ of the PCR ranged from 2 to 4 mm, and $L$ was 5 m. The pressure distribution before and after the PCR was uniform. When air flowed through the PCR of different pore diameters (i.e. $D_P$ = 2, 2.5, 3, 3.5, and 4 mm), it produced different pressure drops (i.e., 180.90, 155.70, 138.81, 124.03, and 110.52 Pa, respectively), as shown in Fig. 4(a–d). The pressure drop decreased as pore diameter increased. Namely, the energy loss caused by fluid flow inside the PCR decreased with pore diameter. The main reason for this phenomenon is that the porous media generates resistance to airflow. A smaller pore size causes more resistance and thus more energy loss and a greater pressure drop.
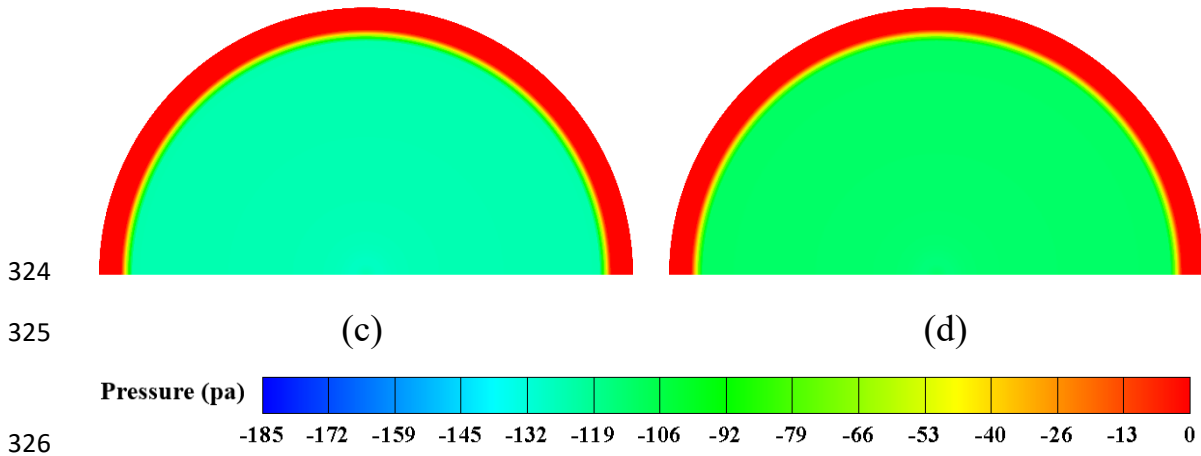


(a)                                              (b)

(c)                                              (d)

**Pressure (pa)**

-185  -172  -159  -145  -132  -119  -106  -92  -79  -66  -53  -40  -26  -13  0
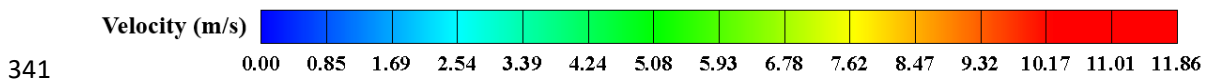
**Fig. 4.** Effect of pore diameter on relative static pressure distributions in the z = 1 face at $L$ =

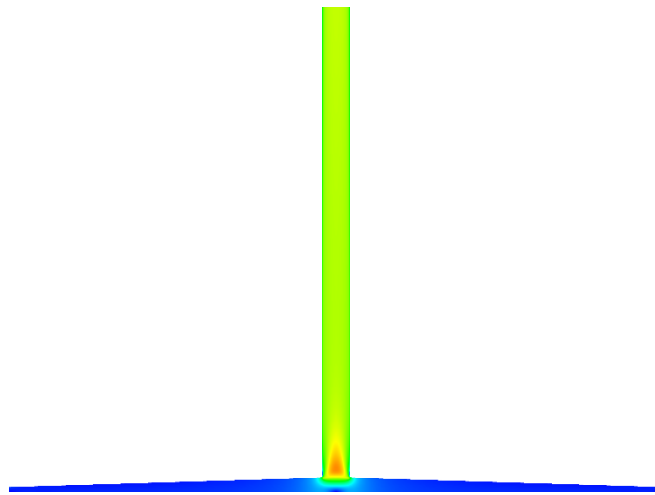5 m. (a) $D_P$ = 2 mm, (b) $D_P$ = 2.5 mm, (c) $D_P$ = 3.5 mm, (d) $D_P$ = 4 mm.

Figure 5 shows a comparison of the contours of the velocity distributions at the symmetry plane (y = 0) under four different pore diameters. The patterns of velocity distribution in the system were similar. Airflow velocity was relatively slow under the collector but increased closer to the center of the chimney. As shown in Fig. 6a–d, the magnitude of the velocity in the system gradually increased with pore diameter.

The ground was heated by solar radiation, and heat converged into the chimney through convective heat transfer with the air under the collector. The updraft reached the maximum velocity at the bottom of the chimney from 10.26 to 11.86 m/s. The updraft velocity decreased gradually inside the chimney and then remained stable along the height. The average velocity at the chimney exit ranged from 7.70 to 8.93 m/s.

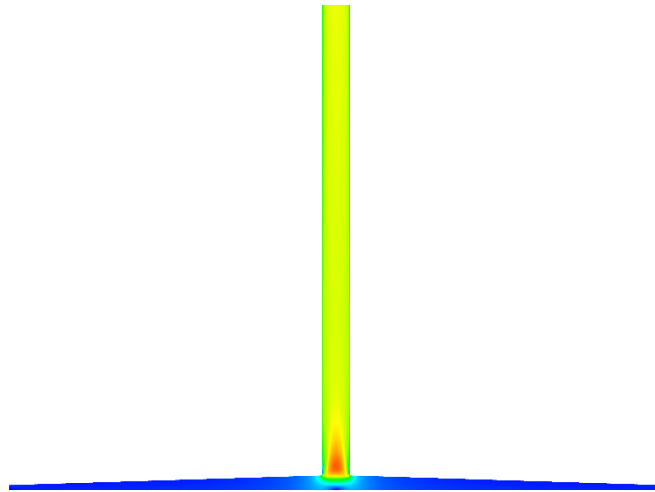**Velocity (m/s)**
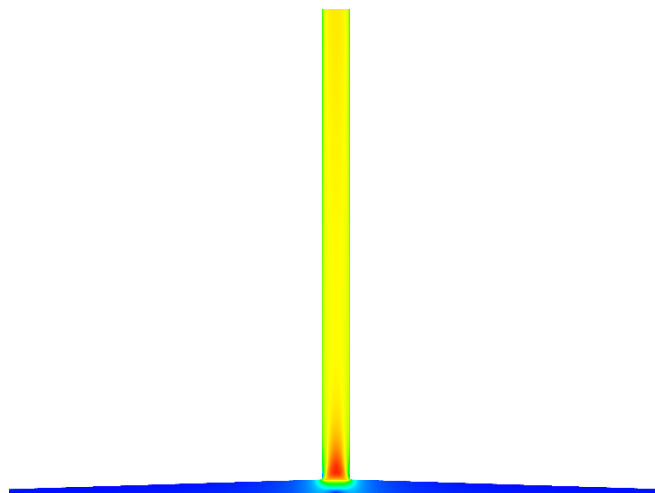
0.00  0.85  1.69  2.54  3.39  4.24  5.08  5.93  6.78  7.62  8.47  9.32  10.17  11.01  11.86

15

342

(a)

344

(b)
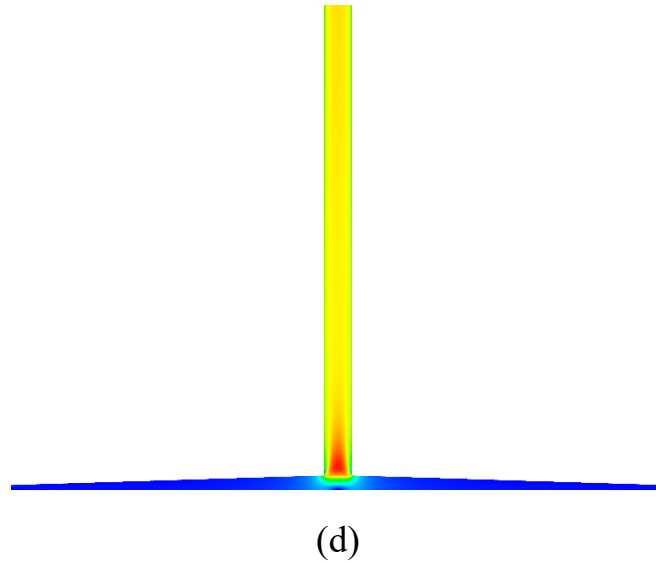
346

(c)

(d)

**Fig. 5.** Contours of velocity distribution in the y = 0 (symmetry) plane with the photoreactor

length $L$ = 5 m. (a) $D_P$ = 2 mm, (b) $D_P$ = 2.5 mm, (c) $D_P$ = 3.5 mm, (d) $D_P$ = 4 mm.


It can be concluded that the pore diameter of the PCR has a strong effect on flow performance, including the pressure drop and flow velocity. A smaller pore diameter produced a higher pressure drop and a slower flow velocity, while a larger pore diameter produced a lower pressure drop and a faster flow velocity.

We also investigated the effect of the other dimension (i.e., PCR length, $L$). Figure 6 denotes the impact of PCR length on the pressure drop. The pressure drop in the PCR increased significantly as PCR length increased, regardless of the pore diameter, which can be explained similarly to that for pore diameter. The porous media generated resistance to airflow. A longer pore channel generated more wall friction and more resistance and more energy lost with a higher pressure drop. The minimum pressure drop was about 80.45 Pa at $D_P$ = 4 mm and $L$ = 3 m, while the maximum pressure drop was 260.02 Pa at $D_P$ = 2 mm and $L$ = 10 m. The total energy loss from the SCPP system alone was mainly from the chimney outlet and the canopy of the collector [47]. The weakening effect of the PCR on the natural convection intensity of the system cannot be ignored in a SCPP-PCR integrated system.

Figure 7 shows the effects of a PCR (with different dimensions) on the velocity and

17

the volume flow rate of the updraft from the chimney outlet. Updraft velocity almost decreased linearly with the increase in PCR length, and it increased with increasing pore diameter. Furthermore, the trend in the volume flow rate at the chimney outlet was consistent with the velocity. For example, when $L$ = 3 m, the updraft velocity and volume flow rate decreased from 9.83 m/s and 772 m$^3$/s to 8.51 m/s and 668 m$^3$/s respectively, with pore diameters from 4 to 2 mm.

In summary, the pore diameter and length of the PCR have significant effects on flow performance, including the pressure drop, flow velocity, and volume flow rate. Shorter PCR lengths or a larger pore diameters produced less reduced convection intensity, such as less of a negative suction effect on the chimney.
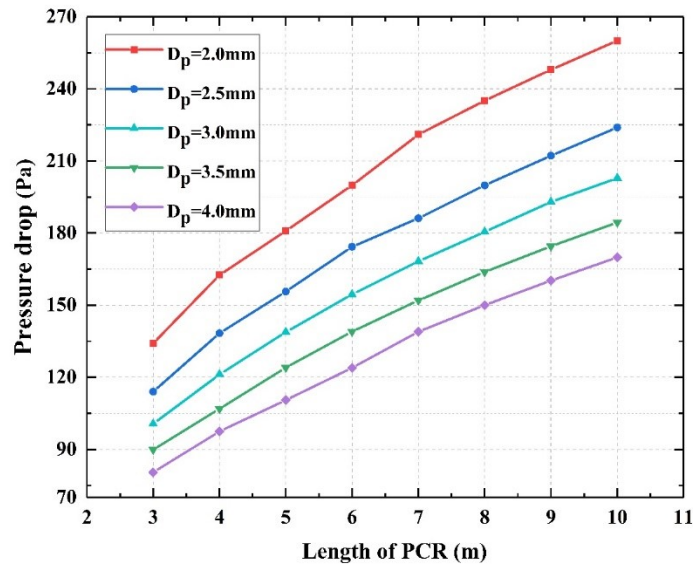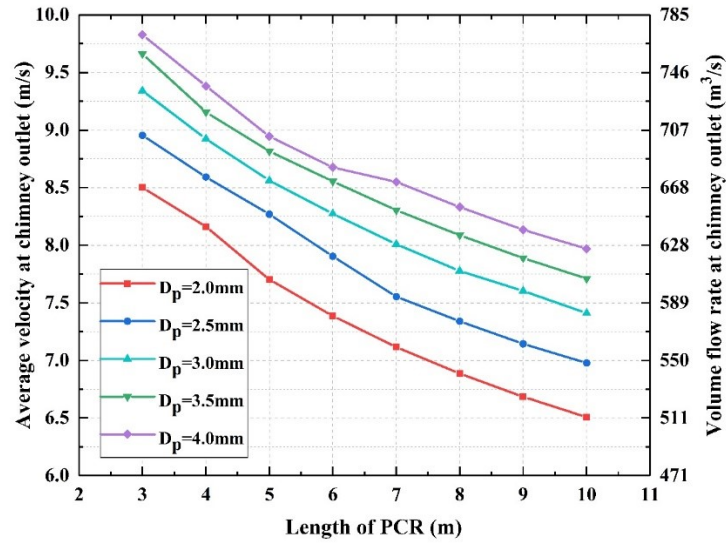


**Fig. 6.** Effect of PCR length on the pressure drop between the inlet and outlet of the PCR at $G$ = 857 W/m$^2$, $\gamma$ = 0.85.

386

### 3.2. Photocatalytic performance

388        Figure 8 shows the methane concentration distribution inside the SCPP-PCR

389    integrated system when the PCR was 5 m in length and with different pore diameters.

390    The methane concentration at the entrance to the collector was 1,886 ppb, which was

391    equal to that in the ambient atmosphere. Taking Figure 8(a) as an example, due to

392    photocatalytic oxidation of methane in the PCR, the methane concentration inside the

393    collector began to decrease gradually at the entrance to the PCR and reached the

394    minimum value at the PCR outlet. Then, air with a reduced methane concentration

395    flowed along the remainder of the collector to the bottom of the chimney due to natural

396    convection. Figure 8 (b) shows the same concentration distribution of methane at the

397    symmetrical plane. The methane concentration inside the chimney remained evenly

398    distributed. The methane concentration was 75 ppb at the chimney outlet. Namely, clean

399    air with only 75 ppb methane was discharged back into the atmosphere.
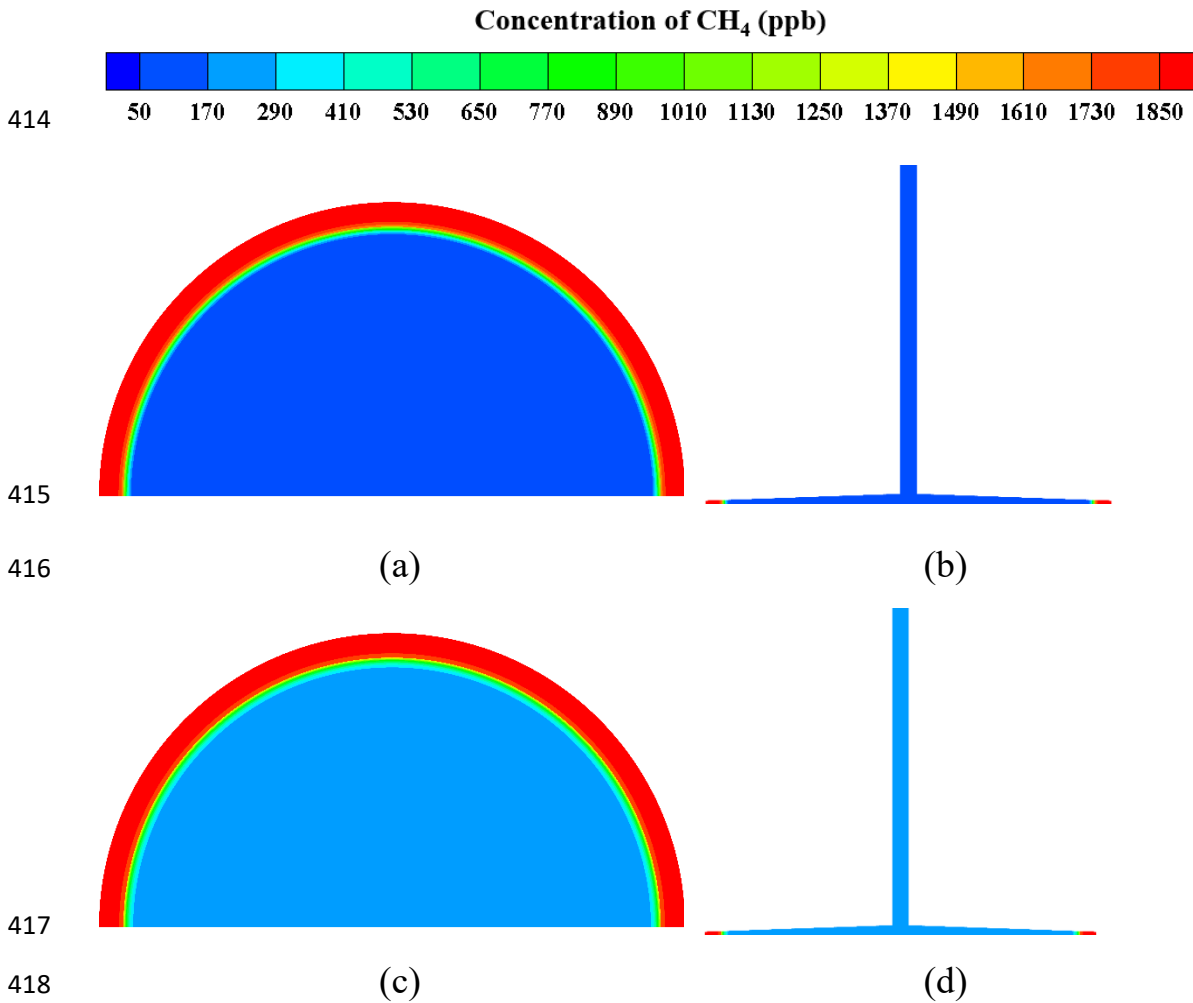
400        The ratio of the methane concentration difference at the inlet and outlet of the

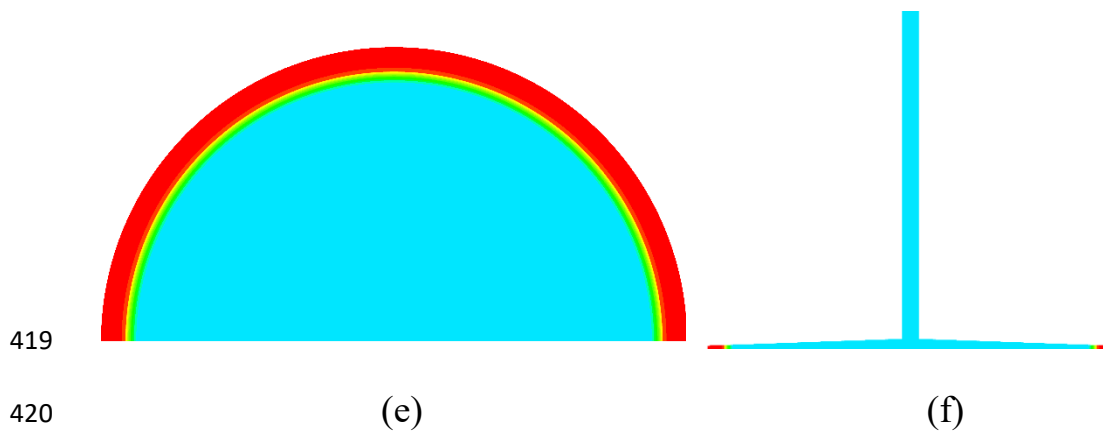401    system to inlet methane concentration was defined as photocatalytic efficiency $E_s$:

402    $E_s = \dfrac{(J_1 - J_2)}{J_1}100\%$                                                    (15)

19

403    where $J_1$ and $J_2$ are the methane concentrations at the entrance and exit of the system,

404    respectively. The photocatalytic efficiency of the system in Fig. 8(a) and (b) was 96.02%

405    when $L = 5$ m and $D_P = 2$ mm.

406         Figure 8(c–f) shows the methane concentration distributions in the SCPP-PCR

407    system with a larger PCR pore diameter. The patterns of distribution were similar to

408    those in Figure 8(a) and (b). The methane concentration at the chimney outlet was 219

409    ppb when $D_P = 3$ mm. The corresponding photocatalytic efficiency was 88.39%. The

410    methane concentration at the chimney outlet was 375 ppb when $D_P = 4$ mm and the

411    corresponding photocatalytic efficiency was 80.11%. Therefore, photocatalytic

412    efficiency decreased with the pore diameter if the PCR length was the same.

413

414



**Concentration of CH$_4$ (ppb)**

50   170   290   410   530   650   770   890   1010   1130   1250   1370   1490   1610   1730   1850

415

416                    (a)                                    (b)

417

418                    (c)                                    (d)

(e)　　　　　　　　　　　　　　(f)

**Fig. 8.** Contours of the methane concentration distribution in the z = 1 m plane and y = 0 (the symmetry) plane with the photoreactor length $L$ = 5 m. (a) $D_P$ = 2 mm, z = 1, (b) $D_P$ = 2 mm, y = 0 (c) $D_P$ = 3 mm, z = 1 (d) $D_P$ = 3 mm, y = 0, (e) $D_P$ = 4 mm, z = 1, (f) $D_P$ = 4 mm, y = 0. Under solar radiation of $G$ = 857 W/m², porosity of $\gamma$ = 0.85.

Next, we investigated the effect of PCR length and pore diameter on photocatalytic performance. Figure 9 shows the photocatalytic efficiency of the system with different PCR dimensions. It is evident that with the increase of PCR length from 3 to 10 m, the photocatalytic efficiency of the system improved at all pore sizes. An increase in PCR length resulted in a larger reaction area and a longer reaction time inside. The increase in the photocatalytic efficiency was not linear. It increased rapidly when the PCR was lengthened from 3 to 4 m and became slower and gradually reached a plateau. This trend was clearer at smaller pore diameters.

It was explained earlier that photocatalytic efficiency was different when pore diameter was changed at a given PCR length. Interestingly, the difference in photocatalytic efficiency caused by different pore diameters was smaller with a longer PCR. When the length of PCR was 10 m, all efficiency values were identical, with a difference of less than 5%. That is to say, when the length of the PCR increased to a certain extent, the change in pore diameter no longer played a crucial role in the catalytic efficiency of the system.

21

441
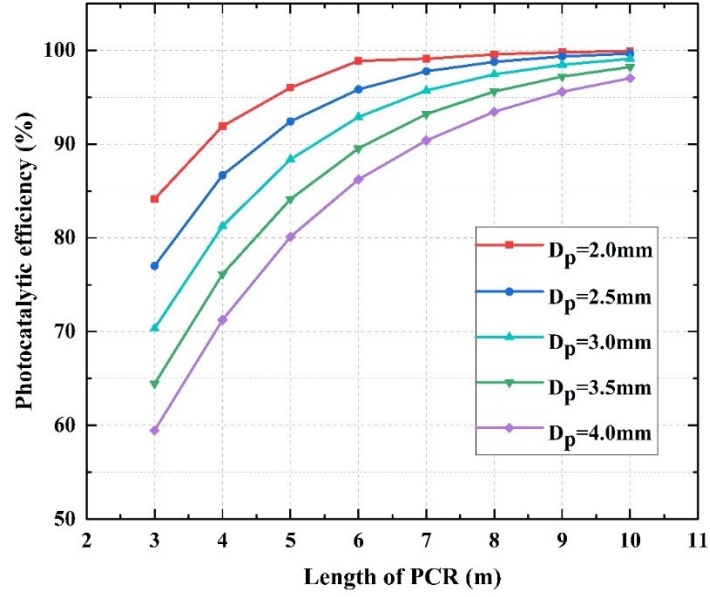
**Fig. 9.** Effect of PCR length on photocatalytic efficiency at $G = 857$ W/m$^2$, $\gamma = 0.85$.



443
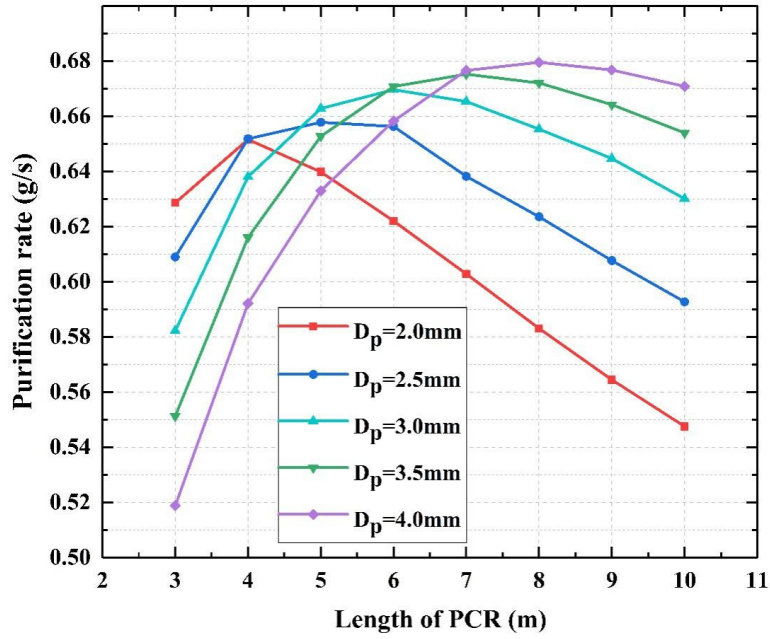
**Fig. 10.** Effect of PCR length on the purification rate at $G = 857$ W/m$^2$, $\gamma = 0.85$.

445

446    More importantly, the amount of methane removed by the SCPP-PCR system is

447    more relevant to GHG removal effectiveness. Thus, we introduced a new evaluation

448    index called the purification rate. The purification rate $R_p$ was defined as:

449        $$R_p = q_m \Delta z \tag{16}$$

22

450 where $\Delta z$ represents the difference of the mass fraction of $CH_4$ between the collector

451 inlet and chimney outlet and $q_m$ is the air mass flow rate of the system flowing through

452 the chimney outlet.

453     Figure 10 shows the relationship between the purification rate of the SCPP-PCR

454 system and the PCR dimensions. Considering $D_P$ = 3 mm as an example, the

455 purification rate climbed from a 3 m long PCR to a 6 m long PCR and then decreased

456 with the increase in length of the PCR. These trends were similar for other pore

457 diameters with different turning points. The influence of the PCR dimensions on the

458 purification rate is a combination of flow rate (Fig.7) and photocatalytic efficiency (Fig.

459 9). In the beginning, the length of the PCR was relatively short, and photocatalytic

460 efficiency improved significantly when length was extended, while the loss of flow rate

461 was not as significant as the improvement in photocatalytic efficiency. Therefore, the

462 overall purification rate increased. When the length of the PCR was extended further,

463 the gain in photocatalytic efficiency was less than the loss in flow rate, and the overall

464 purification rate decreased.

465     As shown in Figure 10, there was a maximum purification rate for each pore

466 diameter. The peak values of $D_P$ = 2, 2.5, 3.0, 3.5, and 4.0 mm appeared respectively

467 at $L$ = 4, 5, 6, 7, and 8 m. The overall optimum was 0.68 g/s of methane removal at

468 $D_P$ = 4.0 mm and $L$ = 8 m.

469 *3.3. Effects of solar radiation*

470     To further discuss the effect of solar radiation on photocatalytic degradation of

471 atmospheric methane and the SCPP-PCR system flow performance, the solar radiation

472 values of the Qianyanzhou area in Taihe County, Jiangxi Province, China on July 24,

473 2016 were adopted for the calculation [48], as shown in Table 2. The mean solar

474 radiation value for every two adjacent hours was taken as an input data for the numerical

475 model, namely, the solar radiation values for the 10 hours from 7:00 a.m. to 5:00 p.m.

476 were divided into five groups (i.e. 372, 776, 889, 808, and 507 W/m$^2$, respectively).

477

478

**Table 3.** Solar radiation data in the Qianyanzhou area, China.

| Time (Local Beijing time) (July 24, 2016) | Solar radiation (60 mins average) (W/m$^2$) | Time (Local Beijing time) (July 24, 2016) | Solar radiation (60 mins average) (W/m$^2$) |
|---|---|---|---|
| 7:00 am-8:00 am | 270 | 12:00 am-1:00 pm | 884.7 |
| 8:00 am-9:00 am | 474 | 1:00 pm-2:00 pm | 889.2 |
| 9:00 am-10:00 am | 715.3 | 2:00 pm-3:00 pm | 716.1 |
| 10:00 am-11:00 am | 837.5 | 3:00 pm-4:00 pm | 607.2 |
| 11:00 am-12:00 am | 892.8 | 4:00 pm-5:00 pm | 407.5 |

479

480    Using $D_P = 4.0$ mm and $L = 8$ m as the PCR dimensions, and porosity was 0.85.

481 Figure 11 displays the changes in velocity and the volume flow rate of the updraft from

482 the chimney outlet under different solar radiation levels. The updraft velocity and the

483 volume flow rate increased with increasing solar radiation. Due to the lower solar

484 irradiation from 7:00 a.m. to 9:00 a.m. and from 3:00 p.m. to 5:00 p.m., airflow inside

485 the system was weaker than at other times of day. Greater solar irradiation generates

486 stronger airflow in the SCPP-PCR system, and the solar irradiation remained relatively

487 strong from 9:00 a.m. to 3:00 p.m. The maximum updraft velocity and volume flow

488 rates were 8.38 m/s and 658 m$^3$/s, corresponding to 11 a.m. to 1 p.m.

489 Figure 12 shows the photocatalytic efficiency and purification rate of the system under

490 different solar radiation levels. Photocatalytic efficiency increased from 82.45% to

491 92.45% with the increase in solar radiation from 372 to 776 W/m$^2$, and photocatalytic

492 efficiency increased by 10%. However, when solar radiation increased from 776 to 889

493 W/m$^2$, photocatalytic efficiency rose < 1.5%. It is evident that after solar radiation

494 reached a specific value, the improvement in photocatalytic efficiency of the system

495 may not be evident with increasing solar radiation. The trend was similar to the
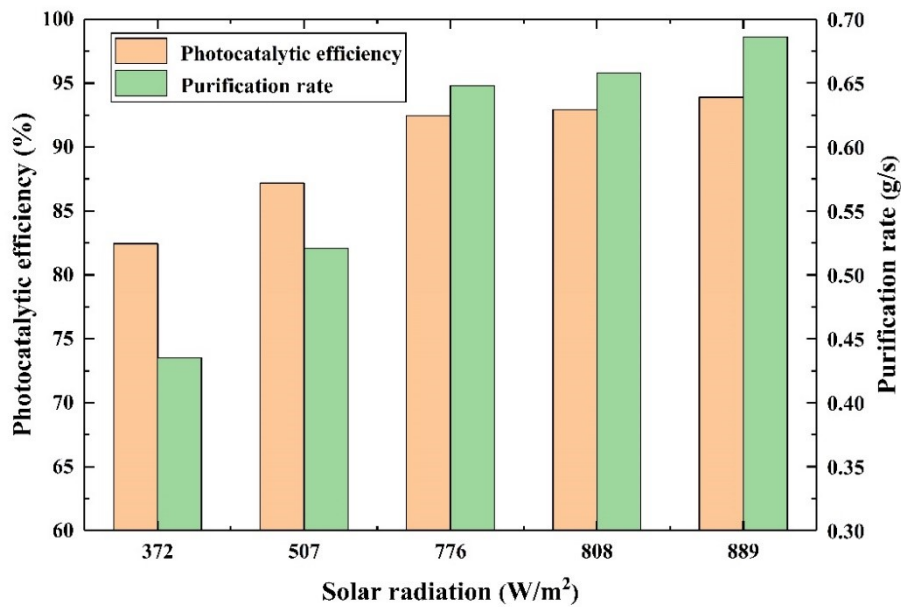
496 purification rate.

497
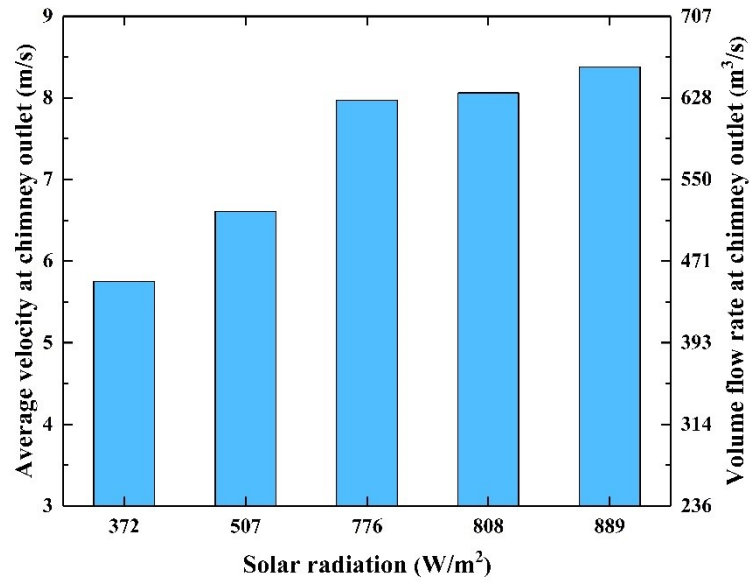
Fig. 11. Effect of solar radiation on average velocity and volume flow rate at the chimney

outlet under $D_P = 4.0$ mm, $L = 8$ m and $\gamma = 0.85$.



500

Fig. 12. Effect of solar radiation on photocatalytic efficiency and the purification rate under

$D_P = 4.0$ mm, $L = 8$ m and $\gamma = 0.85$.

503

In fact, the increased solar radiation strengthened the natural convection to increase

airflow and also increased light intensity in the PCR channel. The maximum photocatalytic efficiency and purification rates were 93.89% and 0.69 g/s, respectively, as shown in Fig. 12.

As shown in Figures 11 and 12, according to the daily solar radiation conditions in the Qianyanzhou area (photocatalysis also occurs under intense sunlight for 10 h/day), the sum of the amount of methane removed by the SCPP-PCR system during these five time periods was calculated. Therefore, methane removal was calculated to be 21,312 g/day (nearly 21 kg/day).

The simulation results show that large-scale degradation of methane in the atmosphere by the SCPP-PCR integrated system is feasible. When the pore diameter of the honeycomb photoreactor was 4 mm, and length was 8 m, the SCPP-PCR system processed 21,312 g of atmospheric methane according to the actual solar radiation data for a particular day. Although the sunlight-driven photocatalysis in the system only operated 10 hours or less per day, the turbine still produces electricity the rest of the time, and some strategies for night operation have been proposed, such as artificial illumination during the night or adding charcoal or biochar to the soil [49]. The choice of dimensions or the type of PCR may also have an effect on the cost. In our further research, we will analyze an integrated system with a turbine to generate power.

## 4. Conclusions

In this study, we proposed a SCPP-PCR system to remove atmospheric-scale $CH_4$ and analyzed the flow properties and photocatalytic performance of the system under various PCR dimensions. The potential to remove $CH_4$ from the atmosphere was demonstrated through our numerical simulations. The approach is highly promising for solving the global warming problem. The numerical simulation results indicate that:

(1) The pore diameter and length of the PCR have the largest effects on flow performance, including pressure drop, flow velocity, and the volume flow rate. A shorter PCR or larger pore diameter produces a smaller pressure drop and a higher flow velocity and volume flow rate.

534 (2) The purification rate of the SCPP-PCR is determined by the system mass flow rate

535 and the photocatalytic efficiency. The overall optimum was 0.68 g/s of methane

536 removal at $D_P = 4.0$ mm and $L = 8$ m.

537 (3) The SCPP-PCR integrated system degraded 21,312 g methane per day under the

538 solar radiation conditions of Qianyanzhou, China, when using a PCR with a pore

539 diameter of 4 mm and length of 8 m.

540

550

551 **References**

552 [1] Greenhouse gas removal. The Royal Society. 2018.

553 [2] Jackson RB, Solomon EI, Canadell JG, Cargnello M, Field CB. Methane removal

554 and atmospheric restoration. Nat Sustain. 2019;2.

555 [3] Li X, Yu J, Jaroniec M, Chen X. Cocatalysts for Selective Photoreduction of CO2

556 into Solar Fuels. Chem Rev. 2019;119(6):3962-4179.

557 [4] Xiang Q, Yu J, Jaroniec M. Graphene-based semiconductor photocatalysts. Chem

558 Soc Rev. 2012;41:782-96.

559 [5] Chen H, Nanayakkara CE, Grassian VH. Titanium dioxide photocatalysis in

560 atmospheric chemistry. Chem Rev. 2012;112:5919-48.

561 [6] Mohamedali M, Ayodele O, Ibrahim H. Challenges and prospects for the

562 photocatalytic liquefaction of methane into oxygenated hydrocarbons. Renew Sustain

Energy Rev. 2020;131:110024.

[7] Krishna V, Kamble VS, Selvam P, Gupta NM. Sunlight-Assisted Photocatalytic Oxidation of Methane over Uranyl-Anchored MCM-41. Catal Lett. 2004;98:113-6.

[8] In SI, Nielsen MG, Vesborg PCK, Hou Y, Abrams BL, Henriksen TR, et al. Photocatalytic methane decomposition over vertically aligned transparent $TiO_2$ nanotube arrays. Chem Commun. 2011;47:2613-5.

[9] Chen X, Li Y, Pan X, Cortie D, Huang X, Yi Z. Photocatalytic oxidation of methane over silver decorated zinc oxide nanocatalysts. Nat Commun. 2016;7:12273.

[10] Guerrini GL. Photocatalytic performances in a city tunnel in Rome: NOx monitoring results. Constr Build Mater. 2012;27:165-75.

[11] Gallus M, Ciuraru R, Mothes F, Akylas V, Barmpas F, Beeldens A, et al. Photocatalytic abatement results from a model street canyon. Environ Sci Pollut R. 2015;22:18185-96.

[12] Yuliati L, Yoshida H. Photocatalytic conversion of methane. Chem Soc Rev. 2008;37:1592-602.

[13] de Richter R, Ming T, Davies P, Liu W, Caillo S. Removal of non-CO2 greenhouse gases by large-scale atmospheric solar photocatalysis. Prog Energ Combust. 2017;60:68-96.

[14] Special Report: Global Warming of 1.5 ºC. Intergovernmental Panel on Climate Change (IPCC). 2018.

[15] Haaf W, Friedrich K, Mayr G, Schlaich J. Solar Chimneys Part I: Principle and Construction of the Pilot Plant in Manzanares. International Journal of Solar Energy. 1983;2(1):3-20.

[16] Guo P, Li T, Xu B, Xu X, Li J. Questions and current understanding about solar chimney power plant: A review. Energy Convers Manage. 2019;182:21-33.

[17] Zhou X, Xu Y. Solar updraft tower power generation. Sol Energy. 2016;128:95-125.

[18] Ming T, Wu Y, de Richter R, Wei L, Sherif SA. Solar updraft power plant system: A brief review and a case study on a new system with radial partition walls in its

592 collector. Renew Sustain Energy Rev. 2017;69:472-87.

593 [19] Kasaeian AB, Molana S, Rahmani K, Wen D. A review on solar chimney systems.

594 Renew Sustain Energy Rev. 2017;67:954-87.

595 [20] Bernardes MADS, Vo A, Weinrebe G. Thermal and technical analyses of solar

596 chimneys. Sol Energy. 2003;75:511-24.

597 [21] Maia CB, Ferreira AG, Valle RM, Cortez MFB. Theoretical evaluation of the

598 influence of geometric parameters and materials on the behavior of the airflow in a solar

599 chimney. Comput Fluids. 2009;38:625-36.

600 [22] Ming T, de Richter R, Meng F, Yuan P, Wei L. Chimney shape numerical study for

601 solar chimney power generating systems. Int J Energ Res. 2013;37:310-22.

602 [23] Guo P, Li J, Wang Y, Wang Y. Evaluation of the optimal turbine pressure drop ratio

603 for a solar chimney power plant. Energy Convers Manage. 2016;108:14-22.

604 [24] Ming T, Gong T, de Richter R, Liu W, Koonsrisuk A. Freshwater generation from

605 a solar chimney power plant. Energy Convers Manage. 2016;113(1):189-200.

606 [25] Wu Y, Ming T, de Richter R, Höffer R, Niemann H-J. Large-scale freshwater

607 generation from the humid air using the modified solar chimney. Renew Energ.

608 2020;146:1325-36.

609 [26] Zhou X, Xu Y, Yuan S, Wu C, Zhang H. Performance and potential of solar updraft

610 tower used as an effective measure to alleviate Chinese urban haze problem. Renew

611 Sustain Energy Rev. 2015;51:1499-1508.

612 [27] Gong T, Ming T, Huang X, de Richter R, Wu Y, Liu W. Numerical analysis on a

613 solar chimney with an inverted U-type cooling tower to mitigate urban air pollution.

614 Sol Energy. 2017;147:68-82.

615 [28] Cao Q, Kuehn TH, Lian S, Chen SC, Zhang N, Yu H, et al. Urban-scale SALSCS,

616 Part I: Experimental Evaluation and Numerical Modeling of a Demonstration Unit.

617 Aerosol Air Qual Res. 2018;18.

618 [29] Zuo L, Ding L, Chen J, Liu Z, Qu N, Zhou X, et al. The effect of different structural

619 parameters on wind supercharged solar chimney power plant combined with seawater

620 desalination. Energy Convers Manage. 2018;176:372-83.

621 [30] Liu Y, Ming T, Wu Y, de Richter R, Fang Y, Zhou N. Desalination of seawater by

622 spray freezing in a natural draft tower. Desalination. 2020;496:114700.

623 [31] Zhou X, Yang J, Bo X, Shi X. Special Climate around a Commercial Solar

624 Chimney Power Plant. J Energ Eng. 2008;134:6-14.

625 [32] Ming T, Liu W, Caillol S. Fighting global warming by climate engineering: Is the

626 Earth radiation management and the solar radiation management any option for fighting

627 climate change? Renew Sustain Energy Rev. 2014;31:792-834.

628 [33] de Richter R, Ming T, Caillol S. Fighting global warming by photocatalytic

629 reduction of CO2 using giant photocatalytic reactors. Renew Sustain Energy Rev.

630 2013;19:82-106.

631 [34] Rui Y . A new method for measuring the reaction coefficients of a photocatalyst. J

632 Eng Thermophys-Rus. 2006;41:1221-9.

633 [35] Hossain MM, Raupp GB, Hay SO, Obee TN. Three-Dimensional Developing Flow

634 Model for Photocatalytic Monolith Reactors. AICHE J. 1999;45:1309-21.

635 [36] Mo J, Zhang Y, Yang R, Xu Q. Influence of fins on formaldehyde removal in

636 annular photocatalytic reactors. Build Environ. 2008;43:238-45.

637 [37] Folli A, Pochard I, Nonat A, Jakobsen UH, Shepherd AM, Macphee DE.

638 Engineering Photocatalytic Cements: Understanding TiO2 Surface Chemistry to

639 Control and Modulate Photocatalytic Performances. J AM Ceram Soc.

640 2010;93(10):3360-3369.

641 [38] Shen W, Ming T, Ding Y, Wu Y, de Richter R. Numerical analysis on an industrial-

642 scaled solar updraft power plant system with ambient crosswind. Renew Energ.

643 2014;68:662-76.

644 [39] Chen Y, Chen W, Pang Y. The Impact Analysis of Air Compressibility in Solar

645 Chimney Power Station. Applied Mechanics and Materials. 2013;283:9-13.

646 [40] Mazumder S, Sengupta D. Sub-grid scale modeling of heterogeneous chemical

647 reactions and transport in full-scale catalytic converters. Combust Flame. 2002;131:85-

648 97.

649 [41] Wang X, Tan X, Yu T. Modeling of Formaldehyde Photocatalytic Degradation in a

Honeycomb Monolith Reactor Using Computational Fluid Dynamics. Ind Eng Chem Res. 2014;53:18402-10.

[42] Haeger A, Kleinschmidt O, Hesse D. Kinetics of Photocatalyzed Gas Reactions Using Titanium Dioxide as the Catalyst Part II: Photocatalyzed Total Oxidation of Alkanes with Oxygen. Chem Eng Technol. 2004;27(9):1019-26.

[43] Ming T, Liu W, Xu G. Analytical and numerical investigation of the solar chimney power plant systems. Int J Energ Res. 2010;30:861-73.

[44] Ming T, Wang X, de Richter R, Liu W, Wu T, Pan Y. Numerical analysis on the influence of ambient crosswind on the performance of solar updraft power plant system. Renew Sustain Energy Rev. 2012;16(8):5567-83.

[45] Xu G, Ming T, Pan Y, Meng F, Zhou C. Numerical analysis on the performance of solar chimney power plant system. Energy Convers Manage. 2011;2011,52(2):876-83.

[46] Haaf W. Solar tower, part ii: Preliminary test results from the manzanares pilot plant. Sol Energy. 1984;2:41-61.

[47] Gannon AJ, Backström TWv. Solar Chimney Cycle Analysis With System Loss and Solar Collector Performance. J Sol Energ-T ASME. 2000;122(3):133-137.

[48] Bai J. Dataset of surface solar radiation and meteorological elements at Qianyanzhouin, Taihe county, Jiangxi Province, China (2013-2016). National Tibetan Plateau Data Center. 2020.

[49] Ming T, de Richter R, Shen S, Caillol S. Fighting global warming by greenhouse gas removal: destroying atmospheric nitrous oxide thanks to synergies between two breakthrough technologies. Environ Sci Pollut R. 2016;23:6119-38.